The Deep-Prior Distribution of Relaxation Times

Journal of The Electrochemical Society, 2020 **167** 026506
1945-7111/2020/167(2)/026506/14/$40.00 © 2020 The Electrochemical Society ("ECS"). Published on behalf of ECS by IOP Publishing Limited

The Deep-Prior Distribution of Relaxation Times

Jiapeng Liu[1] **and Francesco Ciucci**[1,2,*,z]

[1]*Department of Mechanical and Aerospace Engineering, The Hong Kong University of Science and Technology, Hong Kong, People's Republic of China*
[2]*Department of Chemical and Biological Engineering, The Hong Kong University of Science and Technology, Hong Kong, People's Republic of China*

Electrochemical impedance spectroscopy (EIS) is the established tool for the study of many electrochemical experiments. While the analysis of EIS data is challenging, this can be assisted by the distribution of relaxation time (DRT) method. However, obtaining the DRT is difficult as the underlying problem is ill-posed. Inspired by recent advances in image analysis, we develop a completely new approach, named the deep prior distribution of relaxation time (DP-DRT), for the deconvolution of the EIS to obtain the DRT. The DP-DRT uses a deep neural network fed with a single random input to deconvolve the DRT and fit the EIS data. The DP-DRT has the peculiarity of having a number of parameters much larger than the number of observations. Further, unlike most supervised deep learning models, large datasets are not needed as the DP-DRT is trained against a single available EIS spectrum. The DP-DRT was successfully tested against both synthetic and real experiments displaying considerable promise and opportunities for extensions.
 [DOI: 10.1149/1945-7111/ab631a]

Manuscript submitted October 28, 2019; revised manuscript received December 10, 2019. Published January 9, 2020.

Supplementary material for this article is available online

Electrochemical impedance spectroscopy (EIS) is one of the experimental techniques most frequently used in electrochemistry.[1–4] This technique has several well-known strengths. First, it is relatively easy to implement. Second, it gives high precision measurements. And third, it provides data across a wide range of frequencies (from mHz to MHz).[5] For these reasons, this technique has been used in many diverse applications including batteries,[6–10] supercapacitors,[11] solar cells,[12] membranes,[13] electrolyzers,[14] fuel cells,[15,16] medicine,[17] and biology.[18]

In a typical EIS experiment, one takes an electrochemical system at steady-state and perturbs it with a small sinusoidal voltage (or current) with a given frequency. By measuring the current (or voltage) and repeating the same procedure for a given frequency range, the EIS spectrum can be obtained.[1] In short, the EIS technique measures a voltage-to-current transfer function.[5] In spite of the considerable power of this method, it is difficult to interpret EIS data because a model is needed.[19] A common approach is to fit the EIS spectra against networks of elementary circuits. However, one should note that often the circuit networks are just analogs, which may lack uniqueness and physical meaning.[2] Physical models of EIS data would be ideal, but they are problem-specific and can be computationally complex.[20–24] Furthermore, even if a physical model is available, there is no guarantee that it can capture the entire physics of the electrochemical systems at hand. One alternative to these conventional methodologies is to use the distribution of relaxation times (DRT),[25–32] which interprets the impedance as resulting from a distribution of relaxation timescales, i.e.

$$Z_{\text{DRT}}(\gamma,\, f) = if\;\; L_0 + R_\infty + \int_{-\infty}^{\infty} \frac{\gamma(\ln \tau)}{1 + i2\pi f\tau} d\,\ln \tau \qquad [1]$$

where Z_{DRT} is the impedance, f is the frequency, $\gamma(\ln \tau) \geqslant 0$ is the DRT, τ is a timescale variable, R_∞ is a resistance, and L_0 is an inductance. The DRT model has proven to be very powerful, and recently this method has been employed to understand the fundamentals of solid-state ionic systems,[33,34] batteries,[35–38] supercapacitors,[39,40] porous electrochemical reactors,[41] dielectrics,[42] solar cells,[43] and fuel cells.[44–47] These applications have highlighted the promise of DRT models. However, there are still issues. The primary challenge is the estimation of the function $\gamma(\ln \tau)$ because the deconvolution problem is ill-posed and depends very strongly on the experimental errors. To overcome this issue, Fourier,[48,49] evolutionary,[39,50,51] Monte Carlo,[52] maximum entropy,[53] probability-,[54] and regression-based[55–61] inversion methods have been developed. Among these approaches, regularized regression (RR) is perhaps the most popular and efficient. In general terms, RR consists of minimizing, with respect to a vector of DRT values $\boldsymbol{\gamma} = (\gamma(\ln \tau_1), \gamma(\ln \tau_2), \ldots, \gamma(\ln \tau_M))^\top$, a loss function $\mathcal{L}(\boldsymbol{\gamma})$ defined as

$$\mathcal{L}(\gamma,\, \lambda) = \sum_{n=1}^{N} |Z_{\text{exp}}(f_n) - Z_{\text{DRT}}(\gamma, f_n)|^2 + \lambda P(\gamma) \qquad [2]$$

where $Z_{\text{exp}}(f_n)$ is the experimental impedance measured at the frequencies f_n with $n = 1,\ 2, \ldots N$, $Z_{\text{DRT}}(\boldsymbol{\gamma}, f_n)$ is an approximation of (1), and $P(\gamma)$ is some penalty function multiplied by a parameter λ. While RR is relatively well established and can be linked to, and extended by, Bayesian statistics,[62,63] it has the drawback of depending on the parameter λ which biases the estimation of γ.[56] In light of this, more extensions of this method are needed. In this work, we do that by assuming $\boldsymbol{\gamma}$ to be the output of a deep neural network (DNN). We should point the reader that from (1) to (2) the notation of Z_{DRT} changed slightly. In (1), we assumed that the impedance depended on the function $\gamma(\ln \tau)$ and therefore we wrote $Z_{\text{DRT}}(\gamma(\ln \tau), f)$. Instead, in (2) we wrote, consistent with our earlier works,[56,60,62,63] that the impedance of the DRT model depends on the vector $\boldsymbol{\gamma}$, whose entries correspond to the $\gamma(\ln \tau)$ evaluated at certain collocation timescales τ_m with $m = 1,\ 2, \ldots,\ M$. We will use the notation employed in (2) for the remainder of this article.

A seminal work by Ulyanov and co-workers on the deep image prior (DIP) has shown that a DNN with a random input can be trained against a single data point to perform image denoising, inpainting, and super-resolution.[64] The DIP results are particularly striking for two reasons. First, they suggest that a DNN architecture without the pretraining on a large dataset is sufficient for image enhancement. Second, the DNN used by the DIP is heavily over parametrized, and, surprisingly, this property does not prevent improving images.[65] In short, the DIP methodology suggests that the image characteristics (i.e. an image prior) can be directly encoded in the DNN architecture and a training dataset may not be needed for specific problems.[66]

Inspired by the flurry of results following this contribution and, in particular, its application to inverse problems, we adapted the DIP philosophy to develop the deep-prior distribution of relaxation times (DP-DRT).[66–72] In short, we did not assume that N, the number of

*Electrochemical Society Member.
[z]E-mail: francesco.ciucci@ust.hk

frequencies probed experimentally, has the same order of magnitude of the number M, the number of collocation points used to approximate $\gamma(\ln \tau)$. Instead, we took $\boldsymbol{\gamma}$ to be the output of a DNN that depends on a rather large number of parameters. This is shown schematically in Fig. 1, where a DNN depends on (i) a set of weights and biases, which are written as a parameter vector $\boldsymbol{\theta} \in \mathbb{R}^Q$ with $Q \gg N$, M; and (ii) on the chosen activation functions schematically displayed as colored circles. The key idea of the newly developed DP-DRT (DPλ-DRT) is to minimize the loss function (2) with $\lambda = 0$ ($\lambda \geqslant \lambda_0 > 0$ where λ_0 is the lower bound of λ) with respect to the large parameter vector $\boldsymbol{\theta}$ rather than $\boldsymbol{\gamma} \in \mathbb{R}^M$. Using a simple and relatively shallow DNN, we found that the DP-DRT can perform inversion surprisingly well even without regularization. The DP-DRT method can capture overlapping features and discontinuities in the DRT, as well as significant noise in the experimental data. Furthermore, the DP-DRT can deconvolve experimental impedances with outcomes comparable to those of Bayesian methods. These results are particularly remarkable as we did not optimize the DNN architecture in this work.

In the remaining sections, we will first outline the DP-DRT method. Following that, we will show the results obtained with stochastic experiments whose purpose is to assess the consistency and robustness of the approach. Then, the deconvolution results from the DP-DRT of actual real experiments will be discussed and compared to some reference results. Finally, an outlook for future research in this exciting field will be provided.

Theory

The deep distribution of relaxation times.—For the DRT deconvolution, we aim at solving an inverse problem. That is, given an experimental data vector, $\mathbf{Z}_{\text{exp}} = (Z_{\text{exp}}(f_1), Z_{\text{exp}}(f_2), \ldots Z_{\text{exp}}(f_N))^\top$, we want to determine a latent vector $\boldsymbol{\gamma} = (\gamma(\ln \tau_1), \gamma(\ln \tau_2), \ldots, \gamma(\ln \tau_M))^\top$ such that

$$\mathbf{Z}_{\text{exp}} = (\boldsymbol{A}_{\text{re}} + i\,\boldsymbol{A}_{\text{im}})\gamma + \boldsymbol{v} + \boldsymbol{\eta} \qquad [3]$$

where $\boldsymbol{A}_{\text{re}}$ and $\boldsymbol{A}_{\text{im}}$ are suitable matrices described elsewhere,[56] $\boldsymbol{v}$ is a vector-valued function dependent on the two scalar parameters R_∞ and L_0 in (1) (i.e. $\boldsymbol{v} = R_\infty 1 + i\,L_0 \boldsymbol{f}$ with $1 = (1, 1, \ldots, 1)^\top$ and $\boldsymbol{f} = (f_1, f_2, \ldots, f_N)^\top$), and $\boldsymbol{\eta}$ denotes the measurement noise. As already outlined and shown elsewhere,[54,56,60,62,63] this linear model is an approximation of (1). The key contribution of this article is to take γ to be the output of a DNN. γ is a vector-valued function of a random input ζ which depends on a set of parameters $\boldsymbol{\theta} \in \mathbb{R}^Q$ with $Q \gg N$, M.

If R_∞ and L_0 are also outputs of the DNN, i.e., $R_\infty = R_\infty(\zeta, \boldsymbol{\theta})$, $L_0 = L_0(\zeta, \boldsymbol{\theta})$, and $\boldsymbol{v} = \boldsymbol{v}(\zeta, \boldsymbol{\theta})$. We can use (3) to write the loss function (2) as

$$\mathcal{L}(\boldsymbol{\theta}) = \|\mathbf{Z}_{\text{exp}} - (\boldsymbol{A}_{\text{re}} + i\,\boldsymbol{A}_{\text{im}})\boldsymbol{\gamma}(\zeta, \boldsymbol{\theta}) - \boldsymbol{v}(\zeta, \boldsymbol{\theta})\|_2^2 \qquad [4]$$

where $\|\,.\,\|_2$ is the crm.

Implementation.—For all simulations, we set the $\tau = 1/f$ ($M = N$) and chose a relatively simple DNN, see Fig. 1, consisting of 4 layers with (i) a random input ζ; (ii) an output layer of dimension $N + 1$, $N + 2$, or $N + 3$ depending on the total number of parameters outputted (i.e., N for γ and the remaining for R_∞, L_0, and λ); and (iii) 2 hidden layers of the width N. The activation functions were chosen to be non-saturating exponential linear (ELU) units[73] for the first three layers and a softmax ($\beta = 5$) for the last layer. The weights and biases were initialized using the Xavier uniform method[74] and to zero, respectively. Furthermore, the parameters of the network $\boldsymbol{\theta}$ were optimized using the Adam algorithm[75] with a learning rate of 10^{-5} and a maximum of 100,000 iterations. Also, early stopping (i.e. the iterations stop when the absolute value of the variation of the loss is less than 10^{-8}) was used.[76] The input ζ was chosen randomly from a normal distribution with zero mean and unitary standard deviation, i.e. $\zeta \sim \text{N}(0, 1)$. The code was implemented with PyTorch[77] and all simulations were run on a GeForce RTX 2060 GPU.

Stochastic experiments.—The stochastic experiments were generated by corrupting the "exact" impedances with random Gaussian noise, see (3), with

$$\eta = \eta_{\text{re}} + i\,\eta_{\text{im}} \qquad [5]$$

where $(\boldsymbol{\eta}_{\text{re}})_k$ and $(\boldsymbol{\eta}_{\text{im}})_k$ $(k = 1, \cdots, N)$ are independent normal random variables of zero mean and variance σ_n^2, i.e. $(\boldsymbol{\eta}_{\text{re}})_k$, $(\boldsymbol{\eta}_{\text{im}})_k \sim \text{N}(0, \sigma_n^2)$. The chosen frequencies ranged from 10^{-4} to 10^4 Hz with 10 points per decade corresponding to $N = 81$. As already mentioned above, the DRT was evaluated at $\tau = 1/f$, implying that $M = N$. Correspondingly, $Q = 20170$, 20252, or 20334 if the DNN outputs either (γ, R_∞), (γ, R_∞, L_0) or $(\gamma, R_\infty, \lambda)$, or $(\gamma, R_\infty, L_0, \lambda)$, respectively. The models used for the $Z_{\text{exact}}(f)$, the noiseless part of (3), are reported in Table I with the corresponding parameters listed in Table II.

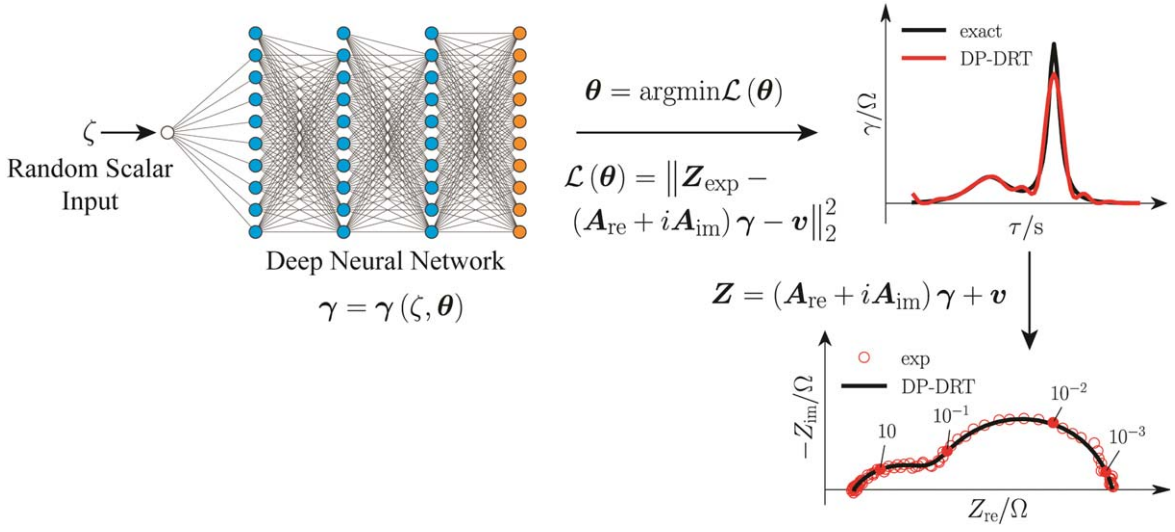

Figure 1. Schematic depiction of the DP-DRT model, a random scalar input is fed into a DNN, regression is used to obtain the network parameters and estimate the impedance. The activation functions are indicated with different colors (blue: ELU; orange: softmax).

Table I. "Exact" impedances and DRTs used in the stochastic experiments.

Model	$Z(f)$	$\gamma(f)$	Notes	Reference
ZARC	$R_\infty + \frac{R_{ct}}{1 + (i2\pi f\tau_0)^\phi}$	$\frac{R_{ct}}{2\pi}\frac{\sin((1-\phi)\pi)}{\cosh\left(\phi \ln\left(\frac{\tau}{\tau_0}\right)\right) - \cos((1-\phi)\pi)}$		[4]
2-ZARCs	$R_\infty + \frac{R_{\text{ct}}}{1 + (i2\pi f\tau_0)^\phi} + \frac{R_{\text{ct}}}{1 + (i2\pi f\tau_1)^\phi}$	$\frac{R_{ct}}{2\pi}\sin((1-\phi)\pi)\left(\frac{1}{\cosh\left(\phi \ln\left(\frac{\tau}{\tau_0}\right)\right) - \cos((1-\phi)\pi)} + \frac{1}{\cosh\left(\phi \ln\left(\frac{\tau}{\tau_1}\right)\right) - \cos((1-\phi)\pi)}\right)$		[4]
Havriliak-Negami	$R_\infty + \frac{R_{\text{ct}}}{(1 + (i2\pi f\tau_0)^\phi)^\psi}$	$\frac{R_{\text{ct}}}{\pi}\frac{\left(\frac{\tau}{\tau_0}\right)^{\phi\psi}\sin(\psi\theta)}{\left(\left(\frac{\tau}{\tau_0}\right)^{2\phi} + 2\left(\frac{\tau}{\tau_0}\right)^{\phi}\cos(\pi\phi) + 1\right)^{\frac{\psi}{2}}}$	$\theta = \arctan\left\lvert\frac{\sin(\pi\phi)}{\left(\frac{\tau}{\tau_0}\right)^{\phi} + \cos(\pi\phi)}\right\rvert$	[78]
Piece-wise Constant	$R_\infty + \frac{R_{\text{ct}}}{\ln\frac{\tau_1}{\tau_0}}\left(\ln\left(1 - \frac{i}{2\pi f\tau_0}\right) - \ln\left(1 - \frac{i}{2\pi f\tau_1}\right)\right)$	$\frac{R_{\text{ct}}}{\ln\frac{\tau_1}{\tau_0}}(H(\tau-\tau_0) - H(\tau-\tau_1))$	$H(\tau)$ is the Heaviside function	[62]
Fractal	$R_\infty + \frac{R_{\text{ct}}}{(1 + i2\pi f\tau_0)^\phi}$	$\gamma(\tau) = \begin{cases}\frac{R_{\text{ct}}}{\pi}\sin(\phi\pi)\left(\frac{\tau}{\tau_0 - \tau}\right)^{\phi} & \text{if } \tau < \tau_0 \\ 0 & \text{otherwise}\end{cases}$		[56]

Table II. Values of the parameters used in the stochastic experiments.

Parameter ZARC	Numerical Value				
	2 ZARCs	Havriliak-Negami	Piecewise Constant	Fractional	
R_∞	10 Ω	10 Ω	10 Ω	10 Ω	10 Ω
R_{ct}	50 Ω	50 Ω	50 Ω	50 Ω	50 Ω
τ_0	1 s	0.1 s	1 s	10 s	1 s
ϕ	0.8	0.8	0.8		0.6
ψ		1 s or 10 s	0.9	0.1 s	

Results

Stochastic experiments.—We conducted stochastic experiments to validate the methodology against cases where impedance, DRT, as well as the noise level, are known. First, we will illustrate the DP-DRT framework. Then, we will show that the method can deconvolve spectra with overlapping timescales. After that, we will discuss the inclusion of a regularizing parameter as the output of the network and analyze the influence of noise level σ_n. Lastly, we will demonstrate that the DP-DRT can deconvolve elements with discontinuous timescale distributions.

An introductory example.—Our investigation started with an illustrative example. We drew the EIS of a single ZARC element with $\sigma_n = 0.1\ \Omega^{\frac{1}{2}}$ as shown in Fig. 2a. Again, the reader can find the analytical formulas and the parameters used in Table I and Table II, respectively. Then, we minimized the loss $\mathcal{L}(\boldsymbol{\theta})$, see (4). The loss, which is plotted as a function of the iteration number (iter) in Fig. 2c, decreases with increasing iteration number and so does the error defined as

$$\text{error(iter)} = \|\boldsymbol{\gamma}(\zeta,\ \theta_{\text{iter}}) - \gamma_{\text{exact}}\|_2 \qquad [6]$$

and shown in Fig. 2d. Two vertical dashed lines are plotted in Fig. 2d and correspond to the early stopping and minimum error or optimal iteration. We also compared the $\gamma(\ln \tau)$'s obtained at those two iterations, see Fig. 2b. Both early-stopping and optimal values are capable of closely matching the EIS and the exact DRT, where

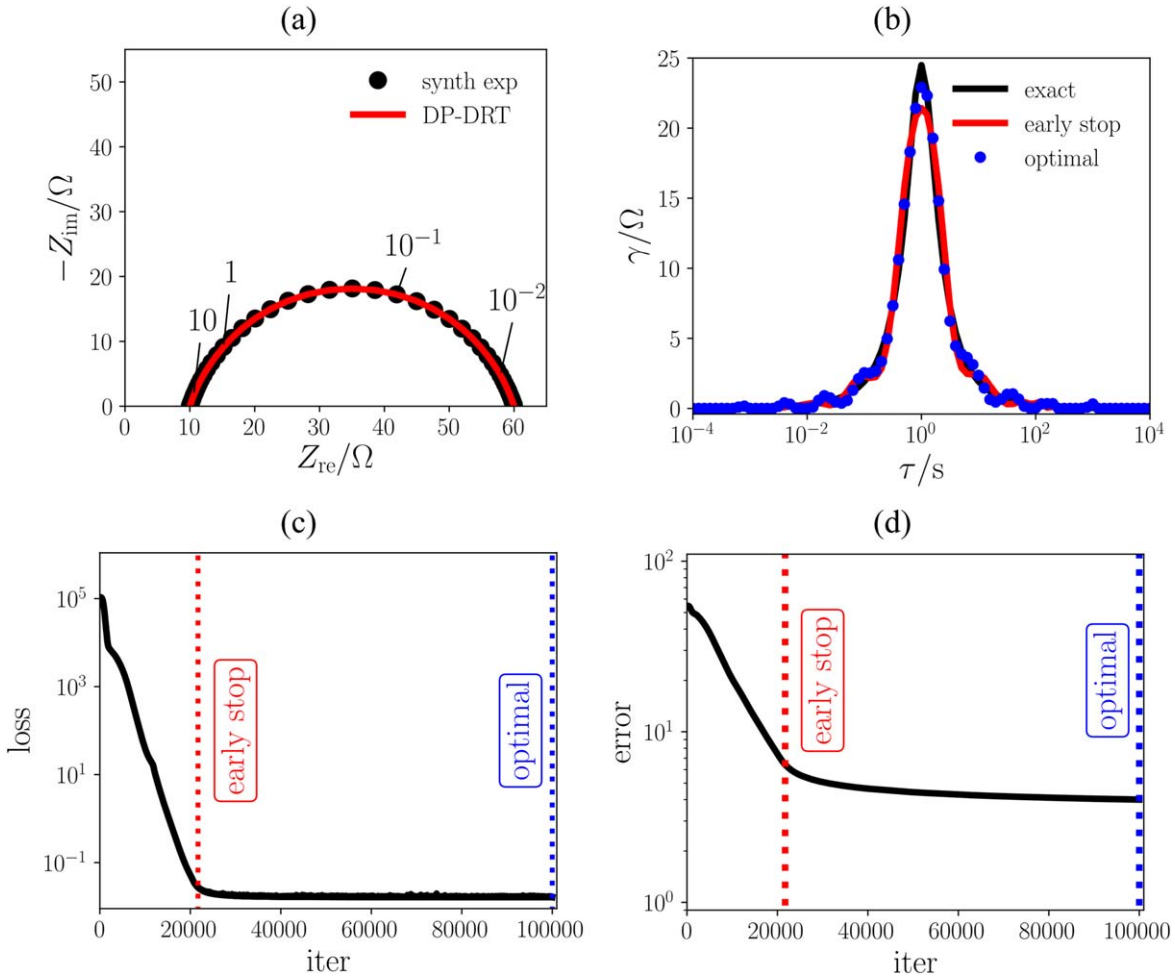

Figure 2. (a) Nyquist plot of the EIS of a circuit consisting of a resistor in series with a single ZARC element (the synthetic experiment and the DP-DRT impedance are shown) and (b) corresponding exact and recovered DRTs. (c) Evolution of the loss and (d) error as a function of iteration number; iteration corresponding to early stopping and minimum error are indicated with the 'early stop' and 'optimal' labels, respectively.

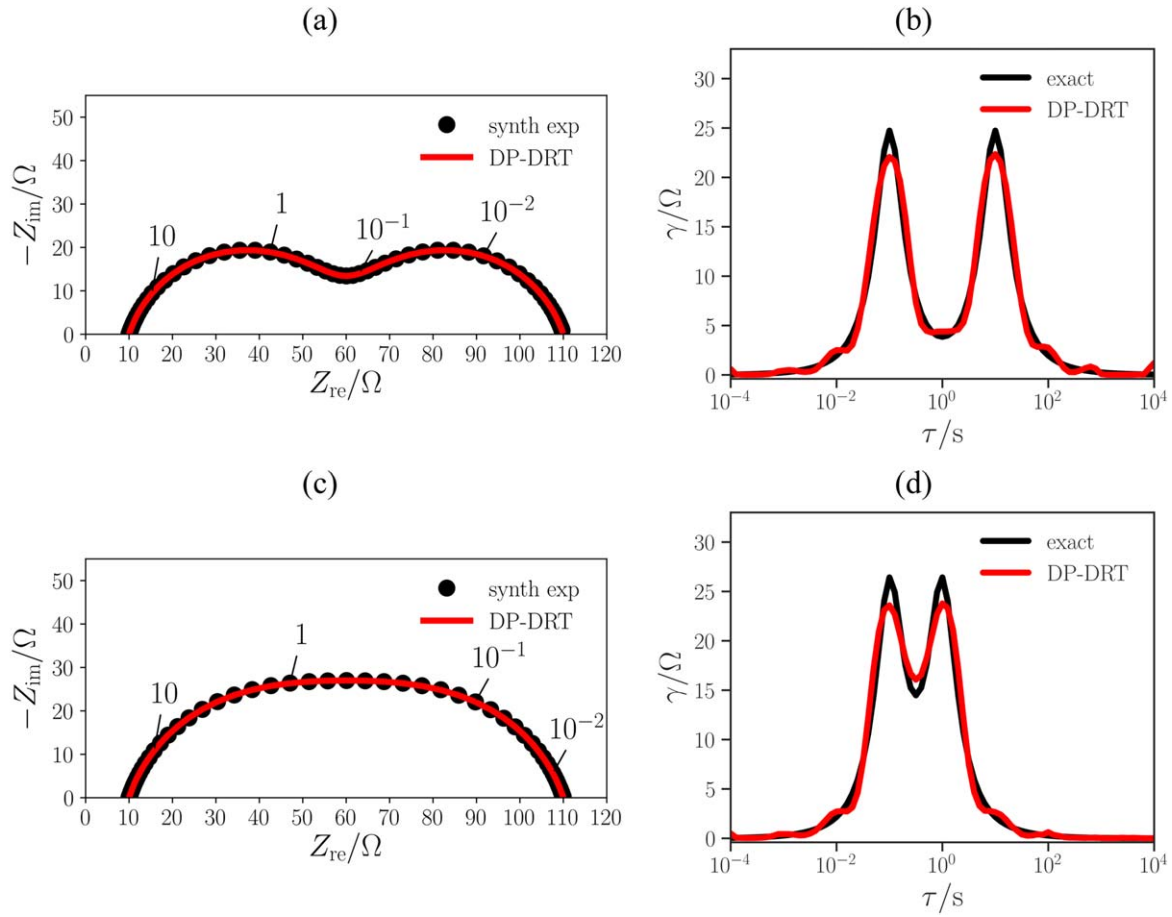

Figure 3. (a) and (c) Nyquist plot of the EIS of a circuit consisting of a resistor in series with two ZARCs. In (b) and (d) the corresponding exact and recovered DRTs are shown.

only small ridges are present at the base of the $\gamma(\ln \tau)$, i.e., for $10^{-2} \leqslant \tau/s \leqslant {}^{1}0^{-1}$ and ${}^{1}0^{1} \leqslant \tau/s \leqslant 10^{2}$.

Overlapping timescales.—We then tested if the method can recover the DRT and EIS of two partially overlapping ZARC elements. The Nyquist plots of the two EIS spectra can be found in Figs. 3a and 3c with the parameters from Table II. The DP-DRT recovers closely the exact EIS. The $\gamma(\ln \tau)$ can be obtained with a similarly limited discrepancy, as shown in Figs. 3b and 3d.

DPλ-DRT: ridge regression with the DP-DRT.—As proposed by Ulyanov and co-workers,[64] adding a regularizing term to the loss can enhance images obtained by the DIP. In that regard, Dittmer and co-workers[68] suggested to output λ from the network itself, where the optimal value is obtained by applying L-curve-like criterion. We attempted to implement a variation of what was proposed in these two articles and added to the loss an approximation of $\gamma(\ln \tau)$'s 2nd derivative.[19,56,62,63] Furthermore, we set $\lambda \geqslant 10^{-6}$. We note that early stopping was still used. As shown in Fig. 4, this procedure leads only to a slight visual improvement in the recovered γ and $\boldsymbol{Z}$ because the regularizing parameter monotonically decreased to 10^{-6} with the number of iterations. A similar improvement cannot be seen if the lower positive bound on λ is not present (i.e. $\lambda \geqslant 0$) as $\lambda \to 0$ with iter $\to \infty$.

Increasing the noise.—One may wonder what happens to the DP-DRT method if the experimental noise intensifies. We have tested this by increasing σ_n by one order of magnitude to $\sigma_n = 1\ \Omega^{\frac{1}{2}}$. This choice leads to heavily corrupted EIS spectra, as shown in Fig. 5a. The DP-DRT method can still recover the function $\gamma(\ln \tau)$ well but a few additional ridges are triggered by the extra noise. It is important to note that, as shown in Fig. 5b, early stopping corresponds to an iteration where the error is near its minimum. As the number of iterations increases, overfitting of $\boldsymbol{Z}$ is expected to occur, leading to an increased error on the latent $\boldsymbol{\gamma}$. If we perform the same procedure with smoothing by using the DPλ-DRT with $\lambda \geqslant 0.1$, the recovered DRT does not show any ridges, see Fig. 5d. However, both the loss and the error increase as shown in Fig. 5f. We must stress that a large λ, i.e., $\lambda \geqslant 0.1$ was chosen in order to emphasize the impact of the regularizing term.

Repeating the same inversion procedure numerous times can help assess the robustness of the approach, which was conducted by performing 1,000 stochastic experiments under the same hypotheses as above. These experiments were followed by DP-DRT inversion with early stopping. In Fig. 6a, we plot the mean DP-DRT and the 5 and 95% confidence bands. It can be observed that the DRT shape is well captured, albeit with some scatter, especially near the peak, indicating strong sensitivity to noise at that location. Further, Fig. 6b plots the probability distribution function (PDF) of the relative error defined as rel. error(iter) $= \|\gamma(\zeta, \boldsymbol{\theta}_{\mathrm{iter}}) - \gamma_{\mathrm{exact}}\|_2 / \|\gamma_{\mathrm{exact}}\|_2$. Consistent with the data shown in Fig. 6a, Fig. 6c indicates that the relative error has a broad distribution. For comparison, Fig. 6b shows the outcome of the DPλ-DRT deconvolution of the same stochastic experiments with the DRT appearing to be smoother. In contrast with the outcome of the DP-DRT (without λ), the recovered $\gamma(\ln \tau)$ is insensitive to the noise, showing a narrow distribution for the relative error, see Fig. 6d. This is consistent with intuition: because of the large additional penalty of $\lambda \geqslant 0.1$, the bias is large, but the variance is small.

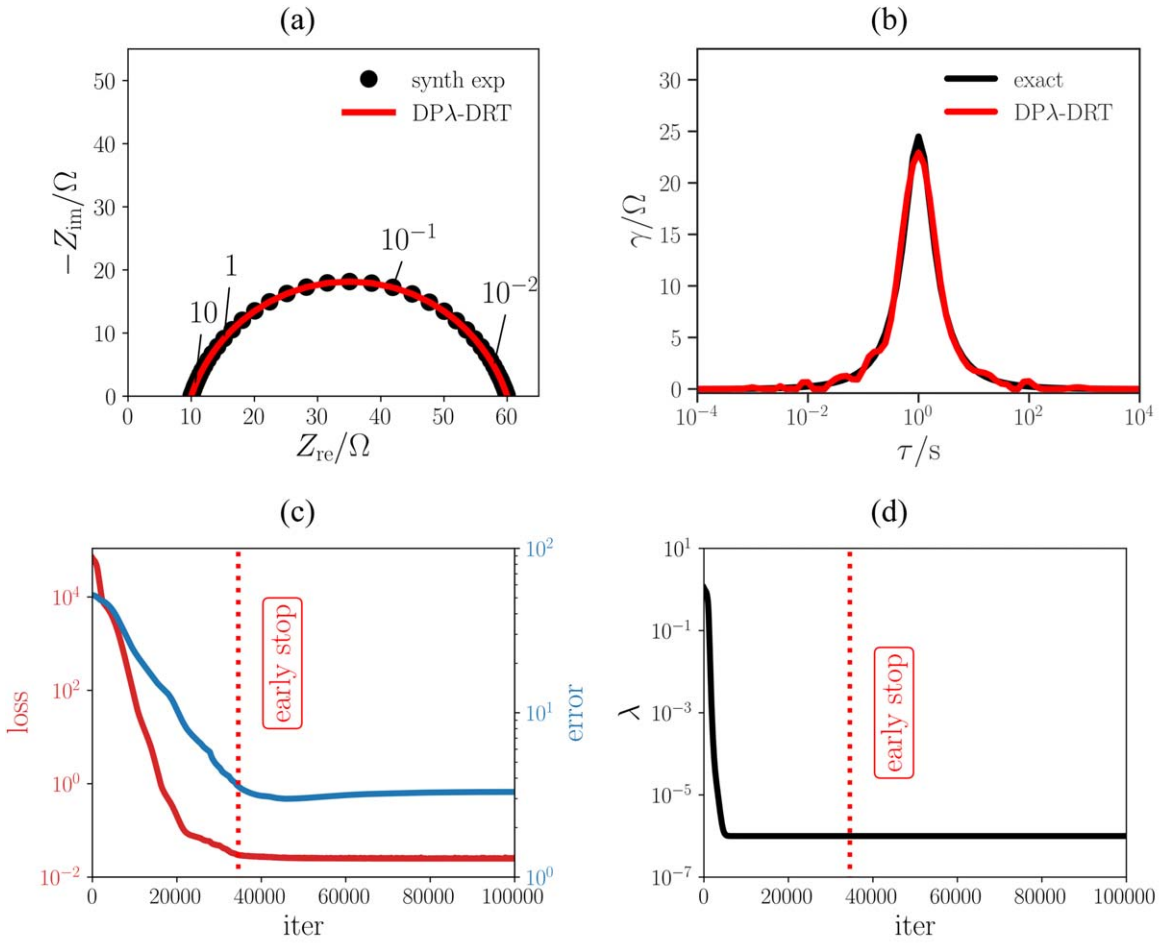

Figure 4. (a) Nyquist plot of the EIS and (b) DRT obtained using the DPλ-DRT method. (c) Evolution of loss and error as a function of iteration with the early stop value shown. (d) Value of λ as outputted by the DNN vs iteration number.

Deconvolving non-conventional distributions of relaxation times.—We also tested whether the DP-DRT method can be used to fit non-conventional elements, whose DRT displays discontinuities and infinite values. For this reason, the EIS was computed for three circuits corresponding to the Havriliak-Negami (HN),[78] piecewise constant (PWC),[62] and fractal[56] models. Then, the 'exact' impedance was corrupted with noise according to (4) with $\sigma_n = 0.1\ \Omega^{\frac{1}{2}}$, see Fig. 7. As shown there, the DP-DRT is able to recover both $Z(f)$ and $\gamma(\ln\tau)$ well. This is evident for the HN and PWC elements, see Figs. 7a–7d. For the fractal element, whose impedance and DRT are shown in Figs. 7e and 7f, respectively, oscillations are visible for $\tau \leqslant 1$ s, though the timescale corresponding to the discontinuity appears to be captured well. We carried out identical stochastic experiments for a higher noise level by increasing σ_n to $0.5\ \Omega^{\frac{1}{2}}$. As reported in Fig. 8, increasing the random experimental error does not affect the recovery of the EIS significantly, but more oscillations appear in the deconvolved $\gamma(\ln\tau)$. These simulation results are consistent with the analysis outlined above.

We also studied the performance of the DP-DRT and DPλ-DRT models for sharp DRTs by choosing similar synthetic experiments as those reported *in An introductory example* where the key differences are the number of collocation point $N = 161$ and ϕ either 0.9 or 0.99. For $\phi = 0.9$, DP-DRT and DPλ-DRT models can match the exact DRT well, Fig. S3. If instead $\phi = 0.99$, the timescale resolution is not sufficient to capture the peak value ($\sim$500 Ω) as shown in Figs. S3d and S4d. Unsurprisingly, $\gamma(\ln\tau)$ obtained by DPλ-DRT deconvolution displays a broader peak width than that from the DP-DRT, see Fig. S5. This difference is due to the penalty used and can be overcome using lasso regularization.[56]

Real experiments.—After testing the consistency of the DP-DRT methodology, we also tested its performance on real experimental data. First, the EIS measurement performed on a symmetrical SOFC cell was analyzed, then the DRT from the EIS of a full Li-ion battery was deconvolved. Depending on whether the regularization term λ is added to the network, the total number of parameters is $Q = 24298$ or 24388, and $Q = 20170$ or 20252 for the SOFC and LIB EIS, respectively.

SOFC cathode.—We first analyzed an EIS spectrum obtained by testing a symmetrical solid oxide fuel cell (SOFC). For comparison, the EIS is repeated in the Nyquist plots shown in Figs. 9a–9c. 15% Samarium-doped ceria was used as the electrolyte and sandwiched between two electrodes consisting of a mixture of Ag and $Ba_{0.9}La_{0.1}FeO_{3-\delta}$.[79] The data was collected at 650 °C in a mixture of N_2 and O_2 ($p_{O_2} = 0.21$ atm) in the frequency range from 0.1 Hz to 8.56×10^4 Hz with 15 points per decade.

We first modeled the experimental data with an equivalent circuit model (ECM) consisting of a ZARC element plus an inductance. The parameters estimated by regression are listed in Table III. The fitted EIS and obtained DRT are shown in Figs. S1a and S1b (available online at stacks.iop.org/JES/167/026506/mmedia), respectively. The EIS obtained by DP-DRT without regularization is shown in Fig. 9a. The corresponding $\gamma(\ln\tau)$ is plotted in Fig. 9d, where, for reference, the DRT of the ECM[54,60] is also shown. The

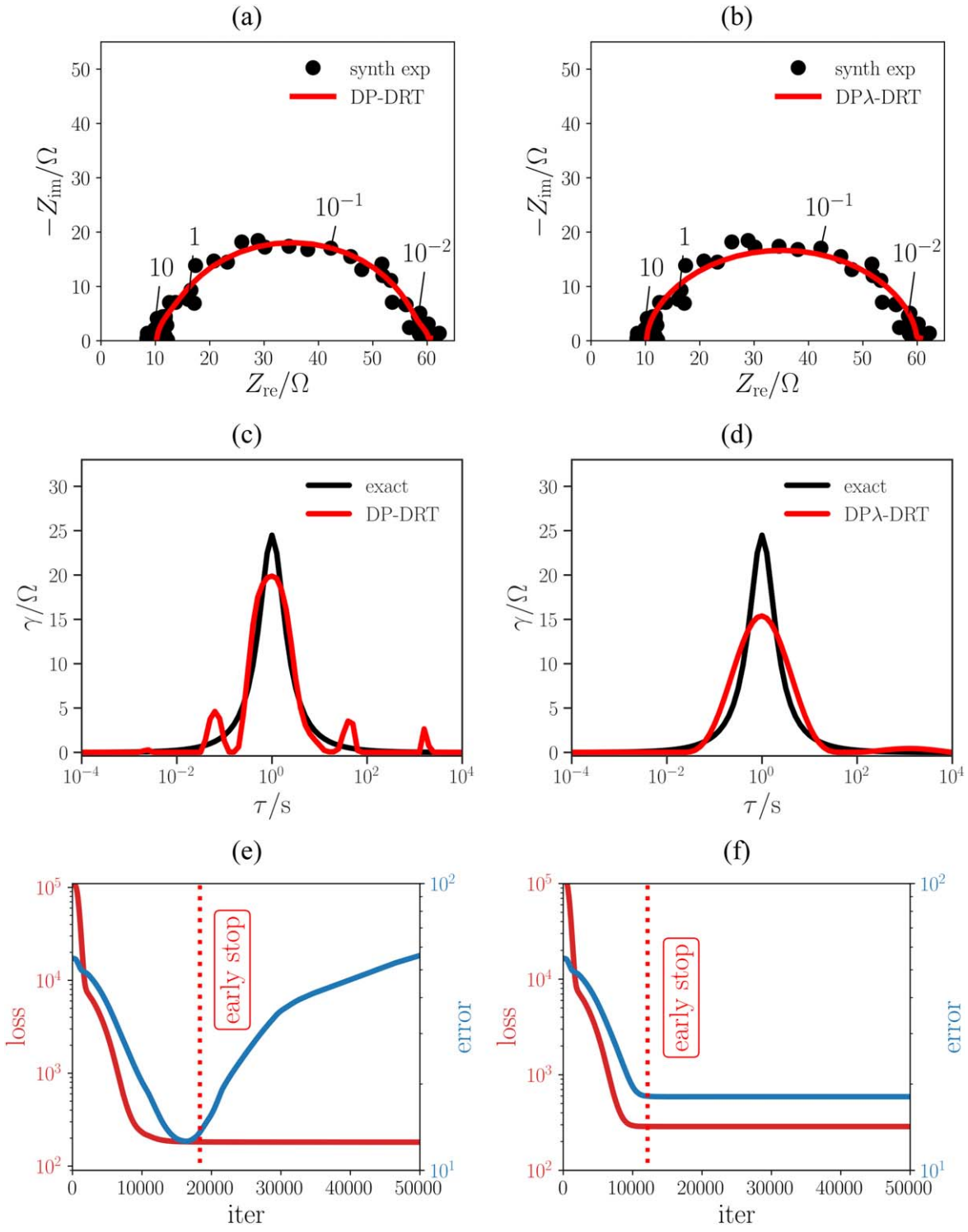

Figure 5. (a) and (b) Noisy EIS ($\sigma_n^{\rm exp} = 1\,\Omega\frac{1}{2}$) and recovery obtained using the DP-DRT and DPλ-DRT ($\lambda \geqslant 0.1$) methods, respectively. (c) and (d) DRT obtained using DP-DRT and DPλ-DRT ($\lambda \geqslant 0.1$) methods, respectively. In (e) and (f), loss and error are shown vs the iteration number; the iteration corresponding to the early stopping is also indicated.

DP-DRT method can recover well both the impedance and the DRT even without regularization. This is shown in Fig. 9g, where the loss (4) and the discrepancy are defined as

$$\text{discrepancy(iter)} = \|\gamma(\zeta,\ \theta_{\textbf{iter}}) - \gamma_{\textbf{ECM}}\|_2 \qquad [7]$$

are plotted as a function of the iteration number. We further report the DPλ-DRT results obtained by setting $\lambda \geqslant 10^{-3}$, see Figs. 9b, 9e, and h, and $\lambda \geqslant 10^{-2}$, see Figs. 9c, 9f, and 9i. Consistent with intuition, the small ridges present in the DP-DRT deconvolution could be smoothed out by including a regularizer. Unsurprisingly, the larger the lower bound on λ is, the more prominent the loss. We should note again that no exact DRT is available, and the discrepancy between DP-DRT and ECM-based distribution serves only as a reference. To compare the performance of different

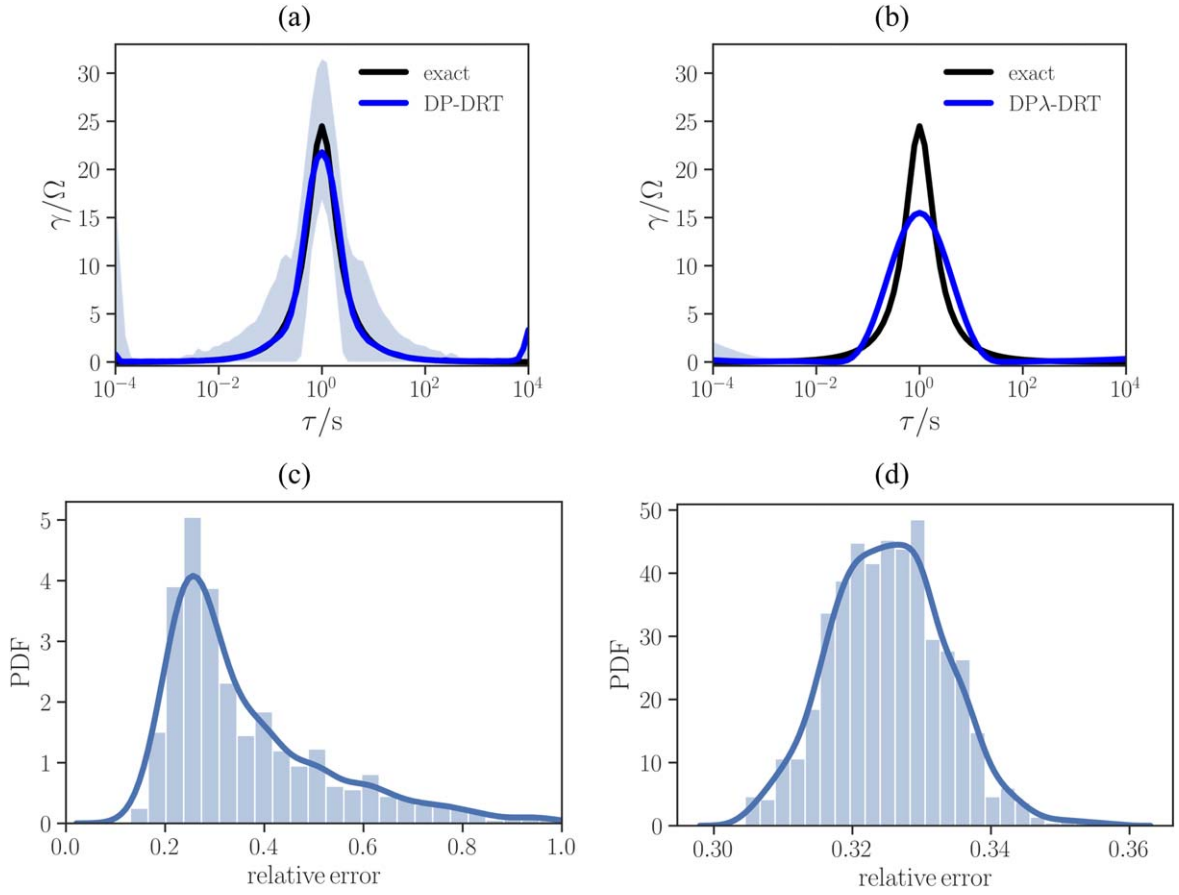

Figure 6. Outcome of 1000 synthetic experiments carried out using an identical setting as the ones shown in Fig. 5. In (a) and (b) the 'exact' DRT is reported together with the average DRT and the corresponding 95% confidence bands as obtained using the DP-DRT and DPλ-DRT ($\lambda \geqslant 0.1$) methods, respectively. (c) and (d), corresponding distributions of the relative errors.

models, we also calculated the mean squared error (MSE) defined as

$$\text{MSE(iter)} = \|Z_{\text{exp}} - Z_{\text{DRT}}\|_2^2 \qquad [8]$$

with the results shown in Table SI. The DP-DRT method performed best with the lowest MSE value. In contrast, the ECM had the largest MSE among all four models.

LIB experiment.—We also tested the DP-DRT model using lithium-ion battery (LIB) data taken from our earlier works.[54,56,63] An ECM consisting of a series of 3 ZARCs and an inductance was used to model the experimental EIS.[54] The parameters of the ECM are listed in Table IV, and the corresponding EIS spectra and DRT are shown in Figs. S2a and S2b, respectively. It is important to note that, as shown in Fig. S2a, the real and imaginary parts of the spectra are in the 0.11 to 0.16 Ω and 0 to 0.016 Ω range, respectively. Since the simulations are carried out in a single-precision floating-point format, the data was scaled to unity to avoid underflow or loss of accuracy. The results were then scaled back to the original values. Similar to the SOFC experiment, the DP-DRT without regularization can fit well to the impedance data, see Fig. 10a. Regarding the DRTs for low enough τ's, the DP-DRT does not have obvious

Table III. Parameters of the ECM (a single ZARC element plus an inductance) used to fit the SOFC experiment and corresponding numerical values obtained by regression. The error of each parameter outputted by ZView is also shown.

Parameter	Regressed value	Error
R_∞	1.81 Ω	4.32×10^{-4} Ω
R_{ct}	0.26 Ω	5.56×10^{-4} Ω
τ_0	2.19×10^{-4} s	1.31×10^{-5} s
ϕ	0.69	2.42×10^{-3}
L_0	5.36×10^{-7} H	1.37×10^{-9} H

Table IV. Parameters of the ECM (3 ZARC elements) used to fit the LIB experiment and corresponding numerical values as obtained by regression. The error of each parameter outputted by ZView is also shown.

Parameter	Regressed value	Error
R_∞	0.11 Ω	4.44×10^{-4} Ω
$R_{\text{ct},1}$	1.69×10^{-2} Ω	8.48×10^{-4} Ω
$R_{\text{ct},2}$	2.12×10^{-2} Ω	4.42×10^{-4} Ω
$R_{\text{ct},3}$	5.23×10^{-2} Ω	1.89×10^{-3} Ω
τ_1	2.34×10^{-3} s	1.23×10^{-3} s
τ_2	0.20 s	1.08×10^{-2} s
τ_3	75.30 s	2.33 s
ϕ_1	0.54	2.31×10^{-2}
ϕ_2	0.94	7.78×10^{-3}
ϕ_3	0.79	1.03×10^{-2}
L_0	7.61×10^{-7} H	3.64×10^{-8} H

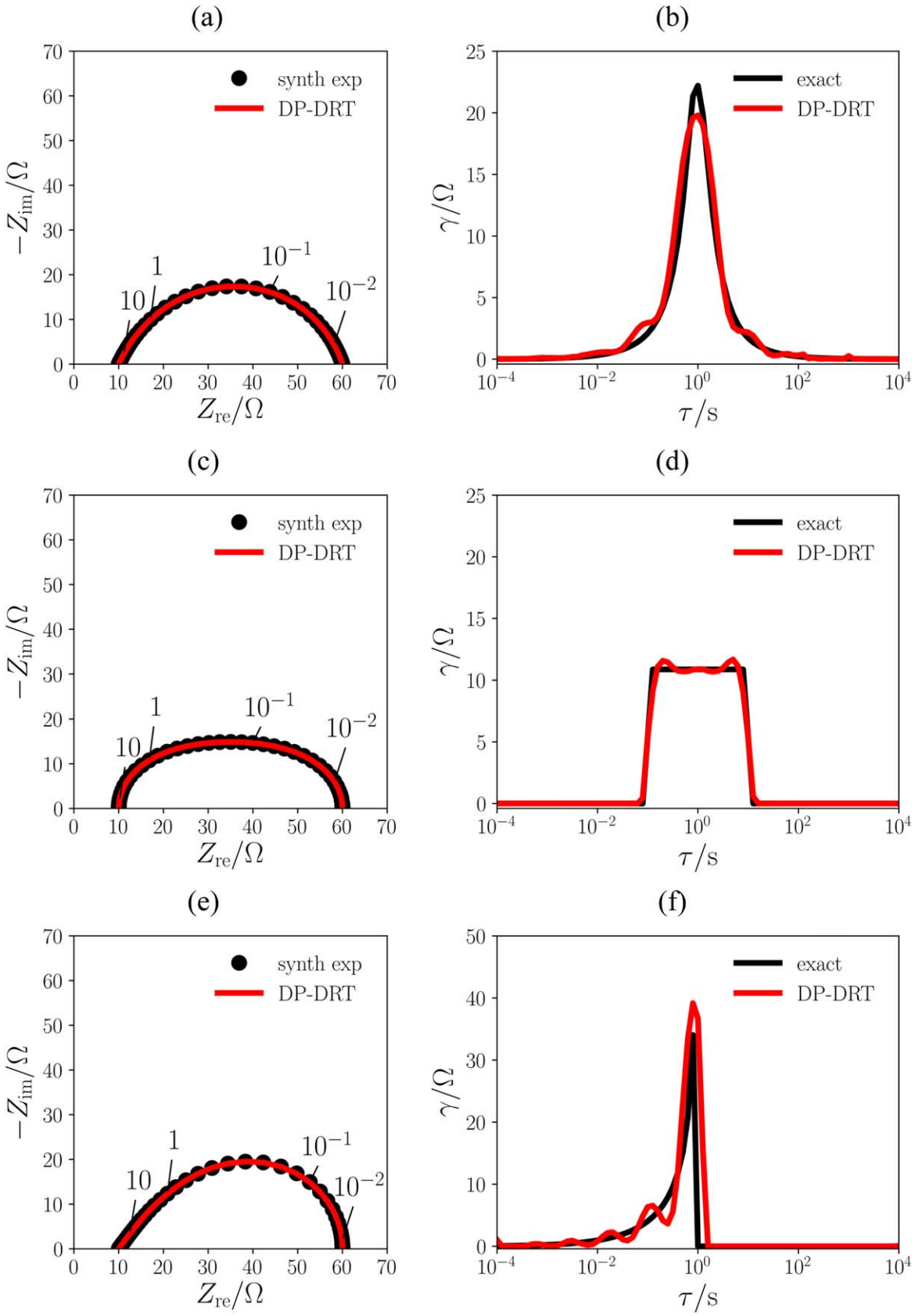

Figure 7. (a), (c), and (e) Nyquist plots of the EIS response of the HN, PWC, and fractal models, respectively. (b), (d), and (f) corresponding DRTs obtained using the DP-DRT method. σ_n^{exp} was set at 0.1 $\Omega^{\frac{1}{2}}$.

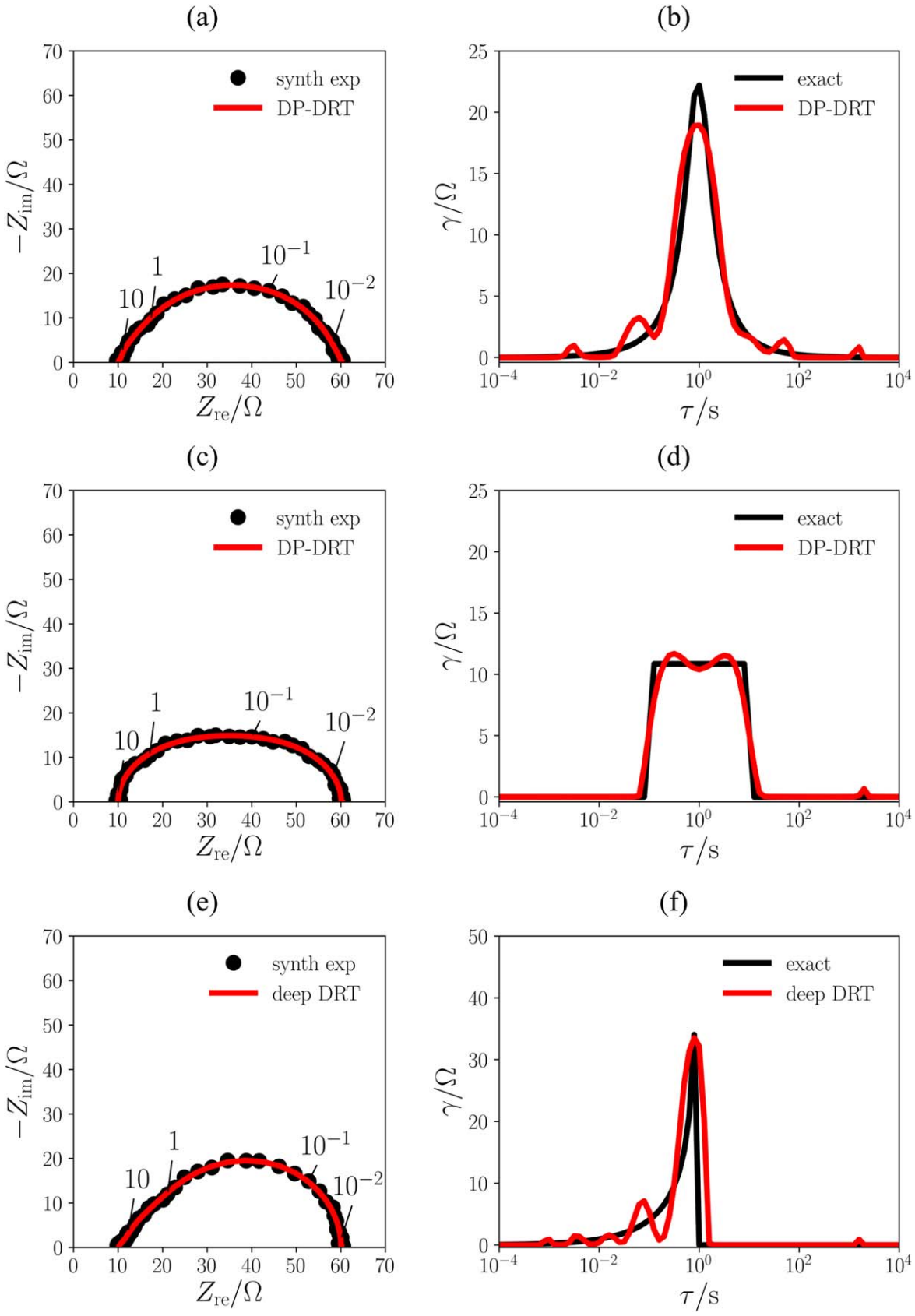

Figure 8. (a), (c), and (e) Nyquist plots of the EIS response of the HN, PWC, and fractal models, respectively. (b), (d), and (f) corresponding DRTs obtained using the DP-DRT approach. σ_n^{exp} was set at 0.5 $\Omega^{\frac{1}{2}}$.

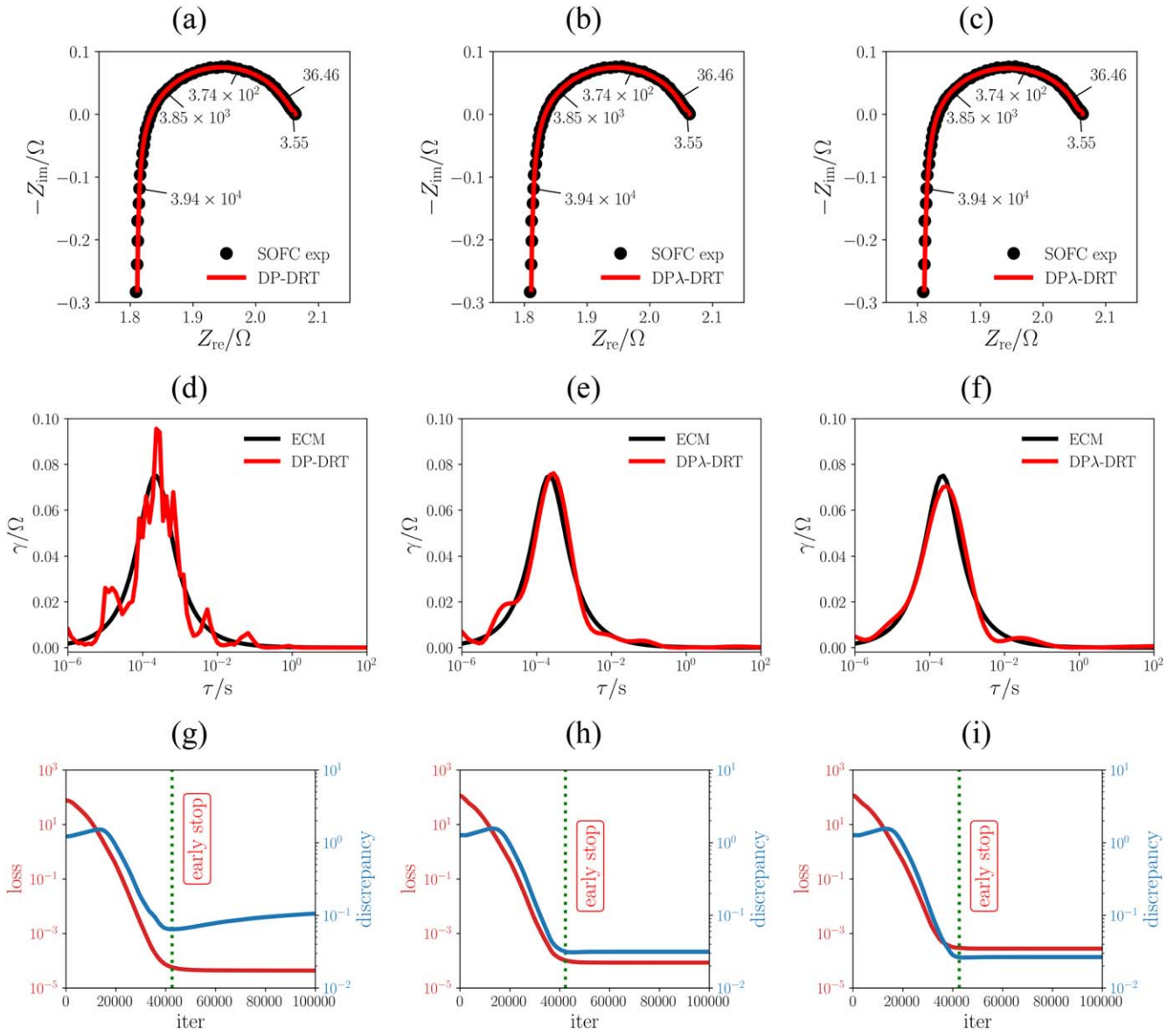

Figure 9. (a), (b), and (c), Nyquist plot of the EIS of the symmetrical SOFC and DP-DRT and DPλ-DRT impedance models shown. (a), (d), and (g) outcome of the DP-DRT deconvolutions. DPλ-DRT model is shown in the remaining panels with $\lambda \geqslant 0.001$ in (b), (e), and (h) and $\lambda \geqslant 0.01$ in (c), (f), and (i). (d), (e), and (f). ECM reference is given in panels (d), (e), and (f). (g), (h), and (i), evolution of the loss and the discrepancy against the ECM reference, the early stopping iteration is indicated with a labeled vertical line.

discrepancies with respect to the DRT reference obtained from the ECM, as the two leftmost peaks of the ECM-DRT can be recovered well, see Fig. 10d. For the rightmost peak, which corresponds to the lowest frequencies probed, and whose corresponding arc is incomplete (see Fig. 10a) the DP-DRT recovery is inconsistent with that obtained with the ECM-based DRT. However, we believe that this is reasonable, especially considering that the uncertainty on any estimate obtained from that part of the EIS spectrum is expected to be high. If the MSE is used as a metric for evaluating the quality of the model, we note that DP-DRT performs better than the ECM, see Table SI.

As conducted for the SOFC deconvolution of subsection 3.2.1, we computed the DPλ-DRT by setting $\lambda \geqslant 10^{-3}$ (Figs. 10b, 10e, and 10h) and $\lambda \geqslant 10^{-2}$ (Figs. 10c, 10f, and 10i). Consistent with our earlier insight, the predicted DRT curves are smoother than without regularization. Further, the loss increases if regularization is included affecting the recovered impedance. We point the reader to Fig. 10c where at around $f \sim 11$ Hz corresponding to the DPλ-DRT with $\lambda \sim 10^{-2}$; deviations in both EIS and DRT can be observed. For the largest λ, the loss and MSE are also the largest among the cases studied, see Fig. 10i and Table S1. It should again be stressed that the DRT obtained from the ECM is only a reference and the "exact" DRT is unknown.

Future Work

We have shown that the DP-DRT model, whose underlying DNN is a function of the network input ζ and is parameterized with respect to $\boldsymbol{\theta} \in \mathbb{R}^Q$ with $Q \gg N$, can recover the EIS and DRT well. Despite the surprising result, several questions remain. For example, can we

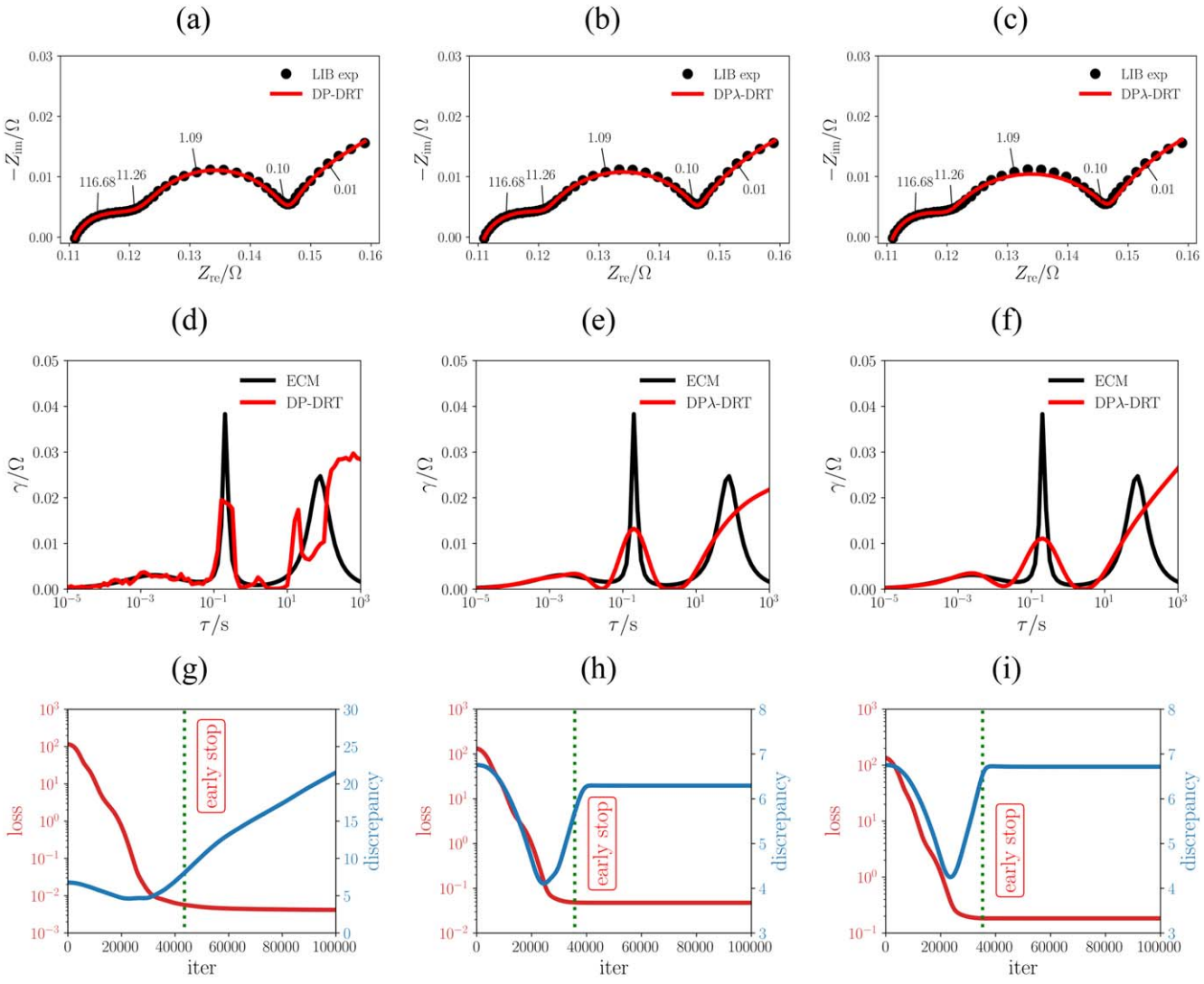

Figure 10. (a), (b), and (c), Nyquist plot of the EIS of the LIB and DP-DRT and DPλ-DRT impedance models shown. (a), (d), and (g), results of the DP-DRT deconvolutions. DPλ-DRT model is shown in panels (b), (e), and (h) with $\lambda \geqslant 0.001$ and in (c), (f), and (i) with $\lambda \geqslant 0.01$. ECM reference is also displayed in (d), (e), and (f). (g), (h), and (i), evolution of the loss and the discrepancy between predicted DRT and the ECM reference, the early stopping is labeled with a vertical line.

optimize the DNN architecture? One potential direction for that would be to include filtering, in the form of a 1D convolutional neural network or a U-net[80] as originally used by Ulyanov and co-workers.[64] Another interesting direction would be the study of under-parametrized networks with $Q \ll N$ as done by Heckel and Hand.[72] In principle, one could obtain a reasonable DRT deconvolution from a network with a scalar random input and a single layer without bias (this corresponds to $Q = N + 1$), as shown in Fig. 11. For that, we tested a single ZARC model as implemented in Fig. 2(a) with $\sigma_n^{\text{exp}} = 0.5\ \Omega^{\frac{1}{2}}$. The inverse problem solution obtained using conventional quadratic programming (QP)[56,60,62] without regularization is shown for reference in Fig. 11a. The results with a single-layer neural network without bias are shown in Figs. 11b, 11c, and 11d, where no activation function, a leaky ReLU activation, and a softplus activation were used, respectively. While the lack of activation function leads to severe oscillations, the inclusion of an activation function together with early stopping has a smoothing effect, allowing the capture of the main peak of the impedance. Starting from these preliminary results, a thorough investigation of the role of DNN architecture, activation function, early stopping cutoff, and single-precision arithmetic should follow the present work.

Conclusions

Here, we report the surprising results that a DNN with a number of parameters much larger than the experimental data can be used for the estimation of the DRT from a single EIS spectrum without pretraining. The DP-DRT method is shown to be able to recover the impedance and its underlying DRT not only for simple elements but also in somewhat pathological situations, for example, when the timescales overlap, noise is significant, and for elements whose DRTs are discontinuous. The DP-DRT approach works well also for real experimental data as it closely matches reference values obtained with other methods.

This article opens up a new way to perform DRT deconvolution as well as opportunities for future works, including improving the DNN architecture, fine-tuning the early stopping criterion, adding ad-hoc regularization, and elucidating the role of single-precision arithmetic on DRT inversion.

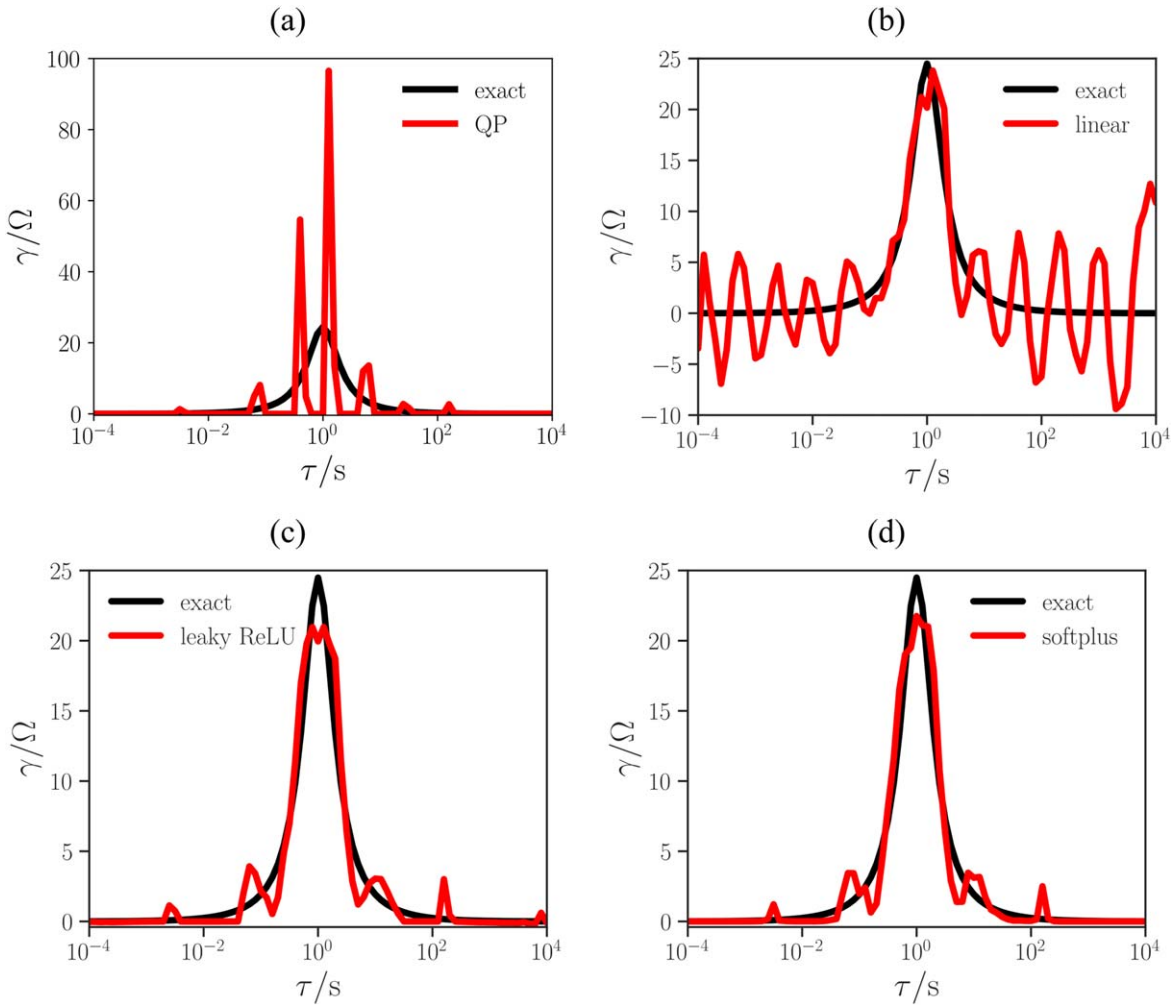

Figure 11. Recovered DRT using (a) the conventional quadratic programming (QP) without penalty, (b), (c), and (d) the DP-DRT method with a single-layer DN. Panels (b), (c), and (d) differ in the activation function, no activation, a leaky-ReLU, and a softplus ($\beta = 1$) activation were used, respectively.

Acknowledgments

The authors gratefully acknowledge the Research Grants Council of Hong Kong for support through the projects (16207615, 16227016, and 16204517). The authors also acknowledge the support from the Guangzhou Science and Technology Program (No. 201807010074), and Hong Kong Innovation and Technology Fund (No. ITS/292/18FP).

References

1. M. E. Orazem and B. Tribollet, in *Electrochemical Impedance Spectroscopy* 2nd ed. (Wiley, New York) (2017).
2. D. D. Macdonald, "Reflections on the history of electrochemical impedance spectroscopy." *Electrochim. Acta*, **51**, 1376 (2006).
3. E. Barsoukov and J. R. Macdonald, in *Impedance Spectroscopy: Theory, Experiment, and Applications* 3rd ed. (Wiley, New York) (2018).
4. A. Lasia, in *Electrochemical Impedance Spectroscopy and its Applications* (Springer, Boston) (2014).
5. A. J. Bard, L. R. Faulkner, J. Leddy, and C. G. Zoski, in *Electrochemical Methods: Fundamentals and Applications* (Wiley, New York) (1980).
6. T. Osaka, D. Mukoyama, and H. Nara, "Review—development of diagnostic process for commercially available batteries, especially lithium ion battery, by electrochemical impedance spectroscopy." *J. Electrochem. Soc.*, **162**, A2529 (2015).
7. J. P. Schmidt, T. Chrobak, M. Ender, J. Illig, D. Klotz, and E. Ivers-Tiffee, "Studies on $LiFePO_4$ as cathode material using impedance spectroscopy." *J. Power Sources*, **196**, 5342 (2011).
8. W. Waag, S. Kabitz, and D. U. Sauer, "Experimental investigation of the lithium-ion battery impedance characteristic at various conditions and aging states and its influence on the application." *Appl. Energy*, **102**, 885 (2013).
9. X. Zhou, Z. Pan, X. Han, L. Lu, and M. Ouyang, "An easy-to-implement multi-point impedance technique for monitoring aging of lithium ion batteries." *J. Power Sources*, **417**, 188 (2019).
10. B. Manikandan, V. Ramar, C. Yap, and P. Balaya, "Investigation of physico-chemical processes in lithium-ion batteries by deconvolution of electrochemical impedance spectra." *J. Power Sources*, **361**, 300 (2017).
11. E. Quattrocchi, T. H. Wan, A. Curcio, S. Pepe, M. B. Effat, and F. Ciucci, "A general model for the impedance of batteries and supercapacitors: the non-linear distribution of diffusion times." *Electrochim. Acta*, **324**, 134853 (2019).
12. P. Wang, Z. Shao, M. Ulfa, and T. Pauporté, "Insights into the hole blocking layer effect on the perovskite solar cell performance and impedance response." *J. Phys. Chem. C*, **121**, 9131 (2017).
13. A. A. Moya, "Electric circuits modelling the low-frequency impedance of ideal ion-exchange membrane systems." *Electrochim. Acta*, **62**, 296 (2012).
14. S. Shit, W. Jang, S. Bolar, N. C. Murmu, H. Koo, and T. Kuila, "Effect of ion diffusion in cobalt molybdenum bimetallic sulfide toward electrocatalytic water splitting." *ACS Appl. Mater. Interfaces*, **11**, 21634 (2019).
15. B. Dolenc, G. Nusev, V. Suboti, C. Hochenauer, N. Gehring, Đ. Juriči, and P. Boškoski, "Fractional-order model identification for state of health assessment of solid-oxide fuel cells." *IFAC-PapersOnLine*, **51**, 849 (2018).
16. M. A. Yatoo, A. Aguadero, and S. J. Skinner, "LaPr3Ni3O9.76 as a candidate solid oxide fuel cell cathode: Role of microstructure and interface structure on electrochemical performance." *Appl. Mater.*, **7**, 013204 (2018).
17. J. Ma et al., "Ultrasonic transducer-guided electrochemical impedance spectroscopy to assess lipid-laden plaques." *Sensors Actuators B*, **235**, 154 (2016).
18. Z. Jiang, J. Yao, L. Wang, H. Wu, J. Huang, T. Zhao, and M. Takei, "Development of a portable electrochemical impedance spectroscopy system for bio-detection." *IEEE Sensors J.*, **19**, 5979 (2019).
19. F. Ciucci, "Modeling electrochemical impedance spectroscopy." *Current Opinion in Electrochemistry*, **13**, 132 (2019).
20. W. Lai and S. M. Haile, "Impedance spectroscopy as a tool for chemical and electrochemical analysis of mixed conductors: a case study of ceria." *J. Am. Ceram. Soc.*, **88**, 2979 (2005).

21. C. Chen, D. Chen, W. C. Chueh, and F. Ciucci, "Modeling the impedance response of mixed-conducting thin film electrodes." *Phys. Chem. Chem. Phys.*, **16**, 11573 (2014).
22. J. Jamnik and J. Maier, "Generalised equivalent circuits for mass and charge transport: chemical capacitance and its implications." *Phys. Chem. Chem. Phys.*, **3**, 1668 (2001).
23. J. Liu and F. Ciucci, "Modeling the impedance spectra of mixed conducting thin films with exposed and embedded current collectors." *Phys. Chem. Chem. Phys.*, **19**, 26310 (2017).
24. R. Drummond, S. Zhao, D. A. Howey, and S. R. Duncan, "Circuit synthesis of electrochemical supercapacitor models." *J. Energy Storage*, **10**, 48 (2017).
25. T. Ivers, E. E. Eacute, and A. Weber, "Eacute, evaluation of electrochemical impedance spectra by the distribution of relaxation times." *J. Ceram. Soc. Jpn.*, **125**, 193 (2017).
26. M. A. Danzer, "Generalized distribution of relaxation times analysis for the characterization of impedance spectra." *Batteries*, **5**, 53 (2019).
27. K. Kobayashi and T. S. Suzuki, "Distribution of relaxation time analysis for non-ideal immittance spectrum: discussion and progress." *J. Phys. Soc. Jpn.*, **87**, 094002 (2018).
28. J. Bartoszek, Y. Liu, J. Karczewski, S. Wang, A. Mrozinski, and P. Jasinski, "Distribution of relaxation times as a method of separation and identification of complex processes measured by impedance spectroscopy." 21st European Microelectronics and Packaging Conf. (EMPC) & Exhibition, 2017 p 1 (2017).
29. X. Zhou, J. Huang, Z. Pan, and M. Ouyang, "Impedance characterization of lithium-ion batteries aging under high-temperature cycling: importance of electrolyte-phase diffusion." *J. Power Sources*, **426**, 216 (2019).
30. G. DiGiuseppe, D. Thompson, C. Gumeci, A. M. Hussain, and N. Dale, "Distribution of relaxation times analysis and interfacial effects of LSCF fired at different temperatures." *Int. J. Hydrogen Energy*, **44**, 27067 (2019).
31. V. Subotić, B. Stoeckl, V. Lawlor, J. Strasser, H. Schroettner, and C. Hochenauer, "Towards a practical tool for online monitoring of solid oxide fuel cell operation: An experimental study and application of advanced data analysis approaches." *Appl. Energy*, **222**, 748 (2018).
32. M. Hahn, S. Schindler, L.-C. Triebs, and A. M. Danzer, "Optimized process parameters for a reproducible distribution of relaxation times analysis of electrochemical systems." *Batteries*, **5** (2019).
33. B. A. Boukamp and A. Rolle, "Analysis and application of distribution of relaxation times in solid state ionics,." *Solid State Ionics*, **302**, 12 (2017).
34. C. Lenser and N. H. Menzler, "Impedance characterization of supported oxygen ion conducting electrolytes." *Solid State Ionics*, **334**, 70 (2019).
35. J. Illig, M. Ender, T. Chrobak, J. P. Schmidt, D. Klotz, and E. Ivers-Tiffée, "Separation of charge transfer and contact resistance in LiFePO4-cathodes by impedance modeling." *J. Electrochem. Soc.*, **159**, A952 (2012).
36. P. Shafiei Sabet, G. Stahl, and D. U. Sauer, "Non-invasive investigation of predominant processes in the impedance spectra of high energy lithium-ion batteries with nickel-cobalt-aluminum cathodes." *J. Power Sources*, **406**, 185 (2018).
37. P. Shafiei Sabet and D. U. Sauer, "Separation of predominant processes in electrochemical impedance spectra of lithium-ion batteries with nickel-manganese-cobalt cathodes." *J. Power Sources*, **425**, 121 (2019).
38. U. Westerhoff, K. Kurbach, F. Lienesch, and M. Kurrat, "Analysis of lithium-ion battery models based on electrochemical impedance spectroscopy." *Energy Technol.*, **4**, 1620 (2016).
39. A. Oz, S. Hershkovitz, and Y. Tsur, "Electrochemical impedance spectroscopy of supercapacitors: a novel analysis approach using evolutionary programming." *AIP Conf. Proc.*, **1627**, 76 (2014).
40. A. Borenstein, S. Hershkovitz, A. Oz, S. Luski, Y. Tsur, and D. Aurbach, "Use of 1,10-phenanthroline as an additive for high-performance supercapacitors." *J. Phys. Chem. C*, **119**, 12165 (2015).
41. S. J. Cooper, A. Bertei, D. P. Finegan, and N. P. Brandon, "Simulated impedance of diffusion in porous media." *Electrochim. Acta*, **251**, 681 (2017).
42. E. Tuncer, "Electrical properties of polyetherimide thin films: Non-parametric dielectric response analysis with distribution of relaxation times." *Eur. Phys. J. E*, **40**, 66 (2017).
43. M. Ahmadi et al., "Environmental gating and galvanic effects in single crystals of organic–inorganic halide perovskites." *ACS Appl. Mater. Interfaces*, **11**, 14722 (2019).
44. A. Weiß, S. Schindler, S. Galbiati, M. A. Danzer, and R. Zeis, "Distribution of relaxation times analysis of high-temperature pem fuel cell impedance spectra." *Electrochim. Acta*, **230**, 391 (2017).
45. B. Stoeckl, V. Subotić, D. Reichholf, H. Schroettner, and C. Hochenauer, "Extensive analysis of large planar SOFC: Operation with humidified methane and carbon monoxide to examine carbon deposition based degradation." *Electrochim. Acta*, **256**, 325 (2017).
46. M. P. Carpanese, D. Clematis, A. Bertei, A. Giuliano, A. Sanson, E. Mercadelli, C. Nicolella, and A. Barbucci, "Understanding the electrochemical behaviour of LSM-based SOFC cathodes. Part I—Experimental and electrochemical." *Solid State Ionics*, **301**, 106 (2017).
47. V. Sonn, A. Leonide, and E. Ivers-Tiffée, "Combined deconvolution and CNLS fitting approach applied on the impedance response of technical Ni/8YSZ cermet electrodes." *J. Electrochem. Soc.*, **155**, B675 (2008).
48. H. Schichlein, A. C. Müller, M. Voigts, A. Krügel, and E. Ivers-Tiffée, "Deconvolution of electrochemical impedance spectra for the identification of electrode reaction mechanisms in solid oxide fuel cells." *J. Appl. Electrochem.*, **32**, 875 (2002).
49. B. A. Boukamp, "Fourier transform distribution function of relaxation times; application and limitations." *Electrochim. Acta*, **154**, 35 (2015).
50. A. Tesler, D. Lewin, S. Baltianski, and Y. Tsur, "Analyzing results of impedance spectroscopy using novel evolutionary programming techniques." *J. Electroceram.*, **24**, 245 (2010).
51. S. Hershkovitz, S. Tomer, S. Baltianski, and Y. Tsur, "ISGP: Impedance spectroscopy analysis using evolutionary programming procedure." *ECS Trans.*, **33**, 67 (2011).
52. E. Tuncer and J. R. Macdonald, "Comparison of methods for estimating continuous distributions of relaxation times." *J. Appl. Phys.*, **99**, 074106 (2006).
53. T. Horlin, "Deconvolution and maximum entropy in impedance spectroscopy of noninductive systems." *Solid State Ionics*, **107**, 241 (1998).
54. J. Liu and F. Ciucci, "The Gaussian process distribution of relaxation times: A machine learning tool for the analysis and prediction of electrochemical impedance spectroscopy data." *Electrochim. Acta*, **331**, 135316 (2020).
55. X. Li, M. Ahmadi, L. Collins, and S. V. Kalinin, "Deconvolving distribution of relaxation times, resistances and inductance from electrochemical impedance spectroscopy via statistical model selection: Exploiting structural-sparsity regularization and data-driven parameter tuning." *Electrochim. Acta*, **313**, 570 (2019).
56. M. Saccoccio, T. H. Wan, C. Chen, and F. Ciucci, "Optimal regularization in distribution of relaxation times applied to electrochemical impedance spectroscopy: ridge and lasso regression methods—a theoretical and experimental study." *Electrochim. Acta*, **147**, 470 (2014).
57. J. R. Macdonald, "Comparison of parametric and nonparametric methods for the analysis and inversion of immittance data: critique of earlier work." *J. Comput. Phys.*, **157**, 280 (2000).
58. A. L. Gavrilyuk, D. A. Osinkin, and D. I. Bronin, "The use of tikhonov regularization method for calculating the distribution function of relaxation times in impedance spectroscopy." *Russ. J. Electrochem.*, **53**, 575 (2017).
59. A. Mertens and J. Granwehr, "Two-dimensional impedance data analysis by the distribution of relaxation times." *J. Energy Storage*, **13**, 401 (2017).
60. T. H. Wan, M. Saccoccio, C. Chen, and F. Ciucci, "Influence of the discretization methods on the distribution of relaxation times deconvolution: implementing radial basis functions with drttools." *Electrochim. Acta*, **184**, 483 (2015).
61. Y. Zhang, Y. Chen, M. Li, M. Yan, M. Ni, and C. Xia, "A high-precision approach to reconstruct distribution of relaxation times from electrochemical impedance spectroscopy." *J. Power Sources*, **308**, 1 (2016).
62. F. Ciucci and C. Chen, "Analysis of electrochemical impedance spectroscopy data using the distribution of relaxation times: a bayesian and hierarchical bayesian approach." *Electrochim. Acta*, **167**, 439 (2015).
63. M. B. Effat and F. Ciucci, "Bayesian and hierarchical bayesian based regularization for deconvolving the distribution of relaxation times from electrochemical impedance spectroscopy data." *Electrochim. Acta*, **247**, 1117 (2017).
64. D. Ulyanov, A. Vedaldi, and V. Lempitsky, "Deep Image Prior." The IEEE Conf. on Computer Vision and Pattern Recognition (CVPR) p 9446 (2018).
65. S. Arridge, P. Maass, O. Öktem, and C.-B. Schönlieb, "Solving inverse problems using data-driven models." *Acta Numer.*, **28**, 1 (2019).
66. Z. Cheng, M. Gadelha, S. Maji, D. Sheldon, and A. Bayesian Perspective, "On the Deep Image Prior."The IEEE Conf. on Computer Vision and Pattern Recognition (CVPR) (2019).
67. G. Mataev, M. Elad, and P. Milanfar, "DeepRED: Deep Image Prior Powered by RED." The IEEE International Conference on Computer Vision (ICCV), 2019.
68. S. Dittmer, T. Kluth, P. Maass, and D. O. Baguer, *Regularization by architecture: A deep prior approach for inverse problems* (2018), arXiv:1812.03889.
69. J. Liu, Y. Sun, X. Xu, and U. S. Kamilov, "Image restoration using total variation regularized deep image prior."ICASSP 2019–2019 IEEE Int. Conf. on Acoustics, Speech and Signal Processing (ICASSP) p 7715, (2019).
70. D. Van Veen, A. Jalal, M. Soltanolkotabi, E. Price, S. Vishwanath, and A. G. Dimakis, *Compressed sensing with deep image prior and learned regularization* (2018), arXiv:1806.06438.
71. Y. Gandelsman, A. Shocher, and M. Irani, "Double-DIP: Unsupervised Image Decomposition via Coupled Deep-Image-Priors."The IEEE Conference on Computer Vision and Pattern Recognition (CVPR) 11026–35 (2019), arXiv:1812.00467.
72. R. Heckel and P. Hand, *Deep Decoder: Concise Image Representations from Untrained Non-convolutional Networks* (2018), arXiv:1810.03982.
73. D.-A. Clevert, T. Unterthiner, and S. Hochreiter, *Fast and Accurate Deep Network Learning by Exponential Linear Units (ELUs)* (2015), arXiv:1511.07289.
74. X. Glorot and Y. Bengio, "Understanding the difficulty of training deep feedforward neural networks."Proc. 13th Int.Conf. on Artificial Intelligence and Statistics p 249, (2010).
75. D. P. Kingma and J. Ba, *Adam: A Method for Stochastic Optimization* (2014), arXiv:1412.6980.
76. L. Prechelt, "Early stopping–but when?" in *Neural Networks: Tricks of the Trade*, ed. G. B. Orr and K.-R. Müller (Springer, Berlin) p 55 (1998).
77. A. Paszke, S. Gross, S. Chintala, G. Chanan, E. Yang, Z. DeVito, Z. Lin, A. Desmaison, L. Antiga, and A. Lerer, "Automatic Differentiation in PyTorch." NIPS Autodiff Workshop, 2017.
78. F. Alvarez, A. Alegra, and J. Colmenero, "Relationship between the time-domain Kohlrausch-Williams-Watts and frequency-domain Havriliak-Negami relaxation functions." *Phys. Rev. B*, **44**, 7306 (1991).
79. J. Liu, J. Wang, A. Belotti, and F. Ciucci, "P-Substituted Ba0.95La0.05FeO3−δ as a Cathode Material for SOFCs." *ACS Appl. Energy Mater.*, **2**, 5472 (2019).
80. O. Ronneberger, P. Fischer, and T. Brox, "U-Net: convolutional networks for biomedical image segmentation." in *Medical Image Computing and Computer-Assisted Intervention–MICCAI 2015*, ed. N. Navab et al. (Springer International Publishing, Cham) p 234 (2015).